

Arrhythmogenicity of cardiac fibrosis: fractal measures and Betti numbers

Mahesh Kumar Mulimani,^{1,*} Brodie A. J. Lawson,^{2,3,†} and Rahul Pandit^{1,‡}

¹Centre for Condensed Matter Theory, Department of Physics,
Indian Institute of Science, Bangalore 560012, India.

²Centre for Data Science, Queensland University of Technology, Brisbane, Australia.

³ARC Centre of Excellence for Mathematical and Statistical Frontiers,
Queensland University of Technology, Brisbane, Australia.

Infarction- or ischaemia-induced cardiac fibrosis can be arrhythmogenic. We use mathematical models for diffuse fibrosis (\mathcal{DF}), interstitial fibrosis (\mathcal{IF}), patchy fibrosis (\mathcal{PF}), and compact fibrosis (\mathcal{CF}) to study patterns of fibrotic cardiac tissue that have been generated by new mathematical algorithms. We show that the fractal dimension \mathbb{D} , the lacunarity \mathcal{L} , and the Betti numbers β_0 and β_1 of such patterns are *fibrotic-tissue markers* that can be used to characterise the arrhythmogenicity of different types of cardiac fibrosis. We hypothesize, and then demonstrate by extensive *in silico* studies of detailed mathematical models for cardiac tissue, that the arrhythmogenicity of fibrotic tissue is high when β_0 is large and the lacunarity parameter b is small.

PACS numbers: 87.19.Xx, 87.15.Aa

Sudden cardiac death (SCD) continues to be a leading cause of death in the industrialised world (see, e.g., Refs. [1–4] and [5]). Even young athletes [6] may be victims of SCD; and a recent study has suggested that there is a correlation between out-of-hospital cardiac arrest and COVID-19 [7, 8]. Ventricular arrhythmias, such as ventricular tachycardia (VT) and ventricular fibrillation (VF), are often the root cause of SCDs [9, 10]. Myocardial infarction and ischaemia lead to *cardiac-tissue fibrosis*, which is one of the important contributors to arrhythmogenesis, and, therefore, to SCDs. Several experimental studies, such as those in Refs. [1, 11, 12], have demonstrated the arrhythmogenicity of cardiac fibrosis, which induces reentry by delaying local conduction. Fibrosis has been observed to alter the dynamics of the electrical waves passing through fibrotic regions; this leads to the formation of re-entrant waves that can precipitate cardiac arrhythmias [13–16].

In the heart, fibrotic tissue is made up of cardiac fibroblast cells or collagen fibers; and it has been classified visually [3, 17] into four different types with (a) diffuse fibrosis (\mathcal{DF}), (b) interstitial fibrosis (\mathcal{IF}), (c) patchy fibrosis (\mathcal{PF}), and (d) compact fibrosis (\mathcal{CF}). However, *in-vivo*, *ex-vivo*, or *in-vitro* studies have not been used hitherto for a quantitative statistical characterization of these types of fibrosis, perhaps because large-enough data sets of images are not available. We show, via detailed analysis, that recently developed mathematical models [18] for fibrotic tissue, which use Perlin noise, and idealised models, which we define below, can be used to distinguish quantitatively between \mathcal{DF} , \mathcal{IF} , \mathcal{CF} , and \mathcal{PF} by obtaining the fractal dimension \mathbb{D} , the lacunarity $\mathcal{L}(\epsilon)$,

and Betti numbers β_0 and β_1 (see, e.g., Refs. [19, 20]) of patterns of fibrotic tissue. For fibrosis patterns, which we obtain from Perlin noise, we employ the notations \mathcal{DFP} , \mathcal{IFP} , \mathcal{CFP} , and \mathcal{PPF} for diffuse, interstitial, patchy, and compact fibrosis, respectively; their counterparts for the idealised model are \mathcal{DFI} , \mathcal{IFI} , \mathcal{CFI} , and \mathcal{PFI} . We show how to compute such properties by the digitisation of images of fibrotic tissue. These properties serve as *fibrotic-tissue markers*; and they can be used to characterise the arrhythmogenicity of different types of cardiac fibrosis. We hypothesize, and then demonstrate by extensive *in silico* studies of detailed mathematical models for cardiac tissue, that the arrhythmogenicity of fibrotic tissue is high when β_0 is large and the lacunarity parameter b is small. Our study has implications for clinical cardiology, because, even at a qualitative level, we find that (a) \mathcal{DF} is most arrhythmogenic and (b) \mathcal{CF} is least arrhythmogenic.

For the dynamics of cardiac myocytes we use the biologically realistic human-ventricular-cell model [21], due to ten Tusscher and Panfilov (henceforth, the TP06 model), in which the spatiotemporal evolution of the transmembrane potential V_m is governed by the following reaction-diffusion partial differential equation (PDE):

$$\frac{\partial V_m}{\partial t} + \frac{I_{ion}}{C_m} = \nabla \cdot (D \nabla V_m); \quad (1)$$

here, I_{ion} is the sum of all the ionic currents (Eq. 2), C_m is the membrane capacitance, and, in the case of tissue with healthy myocytes, we use a scalar diffusion constant $D = 0.00154 \text{ cm}^2/\text{ms}$; in the region of the tissue with fibrosis and with collagenous fibers we use $D = 0$.

$$I_{ion} = I_{Na} + I_{CaL} + I_{to} + I_{Ks} + I_{Kr} + I_{K1} + I_{NaCa} + I_{NaK} + I_{pCa} + I_{pK} + I_{bNa} + I_{bCa}. \quad (2)$$

For the details of the currents we refer the reader to the Ref. [21]; and we use the standard TP06-model parameters [21] for ion-channel conductances. We obtain

* maheshk@iisc.ac.in ;

† brodie.lawson86@gmail.com ;

‡ rahul@iisc.ac.in;

also at Jawaharlal Nehru Centre For Advanced Scientific Research, Jakkur, Bangalore, India

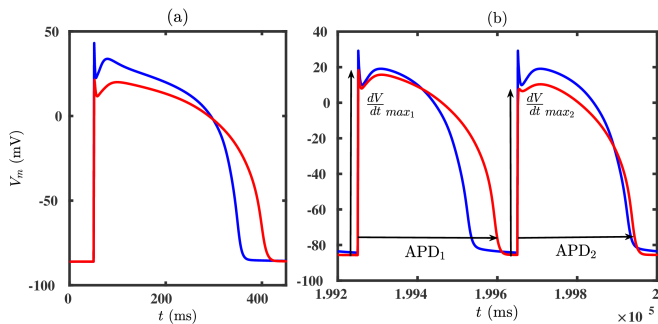


FIG. 1. (Color online) Plots from our simulations of APs of normal (NM) [blue] and remodelled (RM) [red] myocytes: (A) Both the NM and the RM are given a single stimulus pulse; and (B) the 1000th and 999th APs of NM and RM that are paced with a pacing frequency of PCL=400 ms (2.5 Hz); here, we observe alternans for the RM but not for the NM.

the ordinary differential equation (ODE) for a single cardiomyocyte by setting $D = 0$ in Eq. 1. Our model for cardiac tissue has three types of regions:

- those in which we have normal, TP06-model myocytes that evolve according to Eq. 1 with $D = 0.00154 \text{ cm}^2/\text{ms}$;
- in the vicinities of fibrotic areas, there are regions in which remodelled cardiomyocytes evolve according to Eq. 1, with $D = 0.00154 \text{ cm}^2/\text{ms}$, but with modified conductances [we change the maximal ion-channel conductances G_{Na} , G_{CaL} , G_{Kr} and G_{Ks} , in the TP06 model, to $0.38 * G_{Na}$, $0.31 * G_{CaL}$, $0.3 * G_{Kr}$ and $0.2 * G_{Ks}$, respectively, (see, e.g., Ref. [3, 22, 23])];
- fibrotic-tissue regions in which we set $D = 0$.

First we show the effect of remodeling on a single myocyte cell. In Fig. 1 we contrast the action potential (AP) of a normal-myocyte (NM) and a remodelled-myocyte (RM): The upstroke-velocity $\frac{dV}{dt}_{max}$ of the AP decreases and the action-potential duration (APD) increases if we replace a NM by RM. Furthermore, when we pace these myocytes, with a pacing frequency of 2.5 Hz, we observe alternans only in RM. We expect, therefore, that in those parts of the tissue that have RMs the conduction velocity of the wave decreases and its wavelength λ increases. (For the importance of such remodeling, see Fig. S5 in the Supplemental Material [24].)

We use the following two classes of mathematical models for the organization of fibrotic tissue:

- (A) A recently developed model [18] yields fibrotic textures of types \mathcal{DF} , \mathcal{IF} , \mathcal{PF} , and \mathcal{CF} , for which we give illustrative plots in Figs. 2 (a), (b), (c), and (d), respectively, with normal (yellow) and fibrotic (blue) regions. This model creates synthetic textures, for different types of fibrotic tissue, by

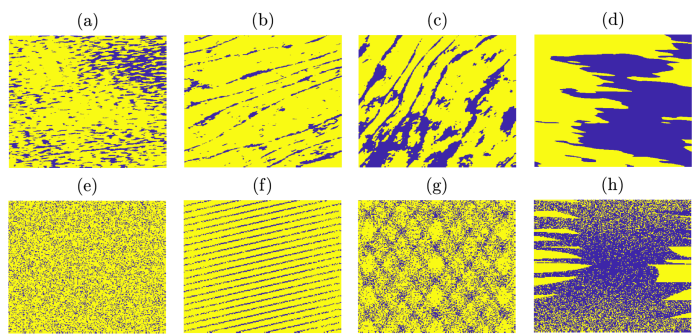


FIG. 2. (Color online) Illustrative plots of fibrotic textures of types (a) \mathcal{DFP} , (b) \mathcal{IFP} , (c) \mathcal{PFP} , and (d) \mathcal{CFP} , from the Perlin-noise model (A) (see text and Ref. [18]); regions with myocytes and with fibrotic tissue are indicated in yellow and blue, respectively. (e) \mathcal{DFI} , (f) \mathcal{IFI} , (g) \mathcal{PFI} , and (g) \mathcal{CFI} in the second row are the counterparts of (a)-(d) for the idealised model (B) (see text).

using Perlin noise and approximate Bayesian computation [18]; these textures match well with those observed in experiments.

- (B) Idealised models, which we define below, in a square region ($R \times R$ grid of myocytes); these models include parameters like p_f , the percentage of fibrotic sites, and $\theta \in [0, \pi]$, the angle that fibrotic strands make with the horizontal axis; these parameters can be tuned easily.
 - (i) \mathcal{DFI} : we replace, randomly, a percentage p_f of myocytes by fibrotic, nonconducting ($D = 0$) sites (Fig. 2 (e));
 - (ii) \mathcal{IFI} : we introduce long, thin strands of non-conducting fibers ($D = 0$), with orientation θ ; fiber thickness: 2 – 3 grid points; fiber lengths go from a minimum of 2 to at most 50 – 60 grid points (Fig. 2 (f)).
 - (iii) \mathcal{PFI} : we use strands, as in \mathcal{IF} , but with two different angles for interstitial fibers, say $\theta_1 = 60^\circ$ and $\theta_2 = 90^\circ + 60^\circ$, with thicknesses and lengths of 2–3 grid points; at the intersection of fibers, we add small patches of diffuse fibrosis with $p_f = 5 - 10\%$ (Fig. 2 (g)).
 - (iv) \mathcal{CFI} : we generate compact regions with random shapes (Fig. 2 (h)) by using the pinta software (Ref. [25]), a program for drawing.

Arrhythmogenicity arises because of the interaction between the wave of electrical activation and the fibrotic tissue. The ratio of the wavelength of this wave and the linear size of the fibrotic tissue is an important control parameter Ref. [26, 27]. We use the following simulation domains: (a) For the Perlin-noise model (A): a square domain with 720×720 grid points; most of the sites in these domains contain normal myocytes, except in a central fibrotic region with 400×250 grid points.

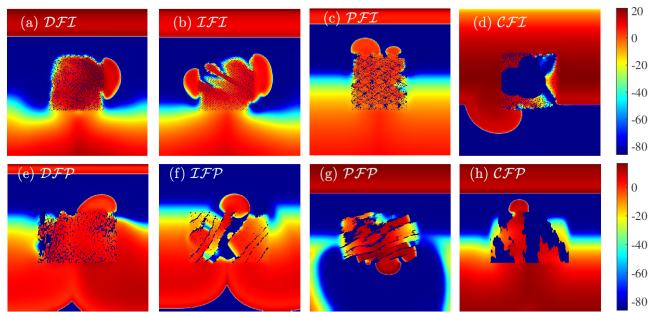


FIG. 3. (Color online) Illustrative pseudocolor plots of V_m when we pace our simulation domain at its lower boundary with a high-frequency ($\omega = 3.3$ Hz) current pulse. (For the full spatiotemporal evolution of V_m see the video V1 in the Supplemental Material [24].) Top row for the idealised model (B): (a) DFI ; (b) IFI ; (c) PFI ; and (d) CFI . Bottom row for the Perlin-noise model (A): (e) DFP ; (f) IFP ; (g) PFP ; and (h) CFP .

(b) For the idealised model (B): a square domain with 512×512 grid points, with normal myocytes, except in a central fibrotic region with 200×200 grid points. The area fractions of fibrotic regions are $\simeq 0.19$ and $\simeq 0.15$ in domains (a) and (b), respectively. In our numerical simulations, we use fixed time and space steps $\Delta t = 0.02$ ms and $\Delta x = 0.025$ cm, respectively, and a finite-difference scheme, with a five-point stencil for the Laplacian in Eq. 1. The value of $D = 0.00154$ cm^2/ms that we use leads to the experimentally observed conduction velocity $CV \simeq 70$ cm/s in a region with normal myocytes [21].

A wave of electrical activation slows down in a region with RMs; this can lead to conduction blocks that are arrhythmogenic. We pace our simulation domain at its lower boundary with a high-frequency ($\omega = 3.3$ Hz) current pulse. The resulting spatiotemporal evolution of V_m , given in the video V1 of the Supplemental Material [24], shows the birth of proto spirals, a clear signature of arrhythmogenesis; we give illustrative pseudocolor plots of V_m in Fig. 3 for DF , IF , PF , and CF in models (A) [top row] and (B) [bottom row].

To quantify the statistical properties of these fibrotic-tissue patterns, we first calculate their fractal dimensions \mathbb{D} and lacunarity $\mathcal{L}(\epsilon)$ (see, e.g., Refs. [19, 20]), at a length scale ϵ , by using, respectively, the *box-counting* and *gliding-box-counting* algorithms [20, 28]. $\mathcal{L}(\epsilon)$, which measures the distribution of the sizes of *lacunae*, the degree of inhomogeneity, and translational and rotational invariance of a pattern [20, 29], is given by

$$\mathcal{L}(\epsilon) = \frac{N(\epsilon)Q_1}{Q_2}, \quad (3)$$

where $N(\epsilon)$ is the number of square boxes of side ϵ , $p(i, \epsilon)$ the number of signal pixels in the i^{th} box with $i \in [1, N(\epsilon)]$, $Q_1 \equiv \sum_i p(i, \epsilon)$, and $Q_2 \equiv \sum_i p(i, \epsilon)^2$. For the values of ϵ we use, we find, as in Ref. [20], that our

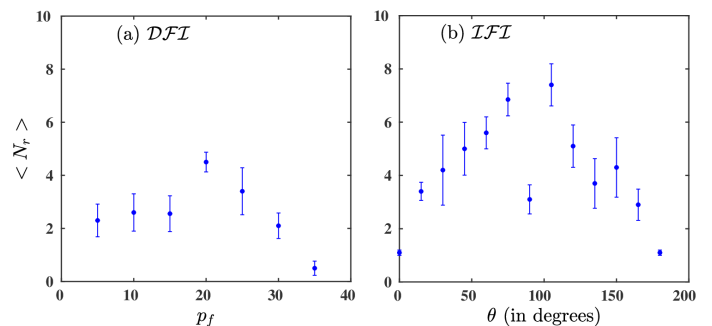


FIG. 4. (Color online) Plots of the mean number $\langle N_r \rangle$ of re-entries that we observe, while pacing the fibrotic tissue with PCL=300 ms in the idealised model (B): (a) versus the percentage p_f of randomly placed fibrotic sites (in DFI); (b) versus the angle θ of the inclination of the fibrotic strands with the pacing plane wave (in IFI).

data can be fit to the form

$$\mathcal{L}(\epsilon) = b \epsilon^{-a}, \quad (4)$$

where b is the *lacunarity parameter* and a is the *lacunarity exponent* (see Figs. S4 and S5 in the Supplemental Material [24]); a small value of b leads to wide concavity in the hyperbolic fit (see Eq. 4). We also characterize these 2D fibrotic textures by their Betti numbers [19] β_0 and β_1 , which measure, respectively, the number of connected components and the number of holes that are completely enclosed by occupied pixels (see Fig.S1 in the Supplemental Material [24]). To obtain β_0 and β_1 , we convert the fibrotic-tissue data sets into the bit-map (bmp) image format; and then we use the computational-homology-project software [30] to get β_0 and β_1 for the particular fibrotic image.

In Fig. 4, we present plots of the mean number $\langle N_r \rangle$ of re-entries that we observe, while pacing the fibrotic tissue with PCL=300 ms in the idealised model (B); these data are averaged over 10 realisations. The larger the value of $\langle N_r \rangle$, the more arrhythmogenic this tissue. In Fig. 4 (a) we plot $\langle N_r \rangle$ versus p_f for DFI ; for $p_f > 35\%$, there is no re-entry because of the very low conduction velocity of the excitations within the fibrotic region; but $\langle N_r \rangle > 0$, for $0\% < p_f \leq 30\%$, so DFI is clearly arrhythmogenic. In Fig. 4 (b) we show how $\langle N_r \rangle$, for IFI , depends on the angle θ of the inclination of the fibrotic strands with the pacing plane wave; $\langle N_r \rangle$ is highest in the range $\theta \simeq 75^\circ - 105^\circ$ and it decreases outside this range. Clearly, θ is an important parameter which determines the arrhythmogenicity of IFI . We find that $\langle N_r \rangle$ in PFI is comparable to that in IFI . By contrast, CFI shows much lower values of $\langle N_r \rangle$ than the other types of fibrotic patterns.

In Fig. 5 we present, for the Perlin-noise model (A), plots versus the realisation number $r = 1, 2, \dots, 955$ of the fractal dimension \mathbb{D} (left panel) and the lacunarity parameter (right panel) b , defined in Eq. 4, for all types of fibrotic regions, namely, DFP (blue), IFP (red), PFP

(black), and \mathcal{CFP} (pink); we use angular brackets for mean values. We see from these plots that \mathbb{D} is the same (within error bars) for \mathcal{DFP} and \mathcal{PFP} ; however, these four different fibrotic patterns are distinguished clearly by their lacunarity parameters b .

In Fig. 6 we present, in the top row, plots versus the realisation number $r = 1, 2, \dots, 955$, for the Perlin-noise model (A), of the Betti numbers β_0 (blue) and β_1 (red) for (a) \mathcal{DFP} , (b) \mathcal{IFP} , (c) \mathcal{PFP} , and (d) \mathcal{CFP} ; we use angular brackets for mean values. In the bottom row of Fig. 6 we give histograms of N_r , which we obtain from 150 model-(A) realizations of the fibrotic regions \mathcal{DFP} , \mathcal{IFP} , \mathcal{PFP} , and \mathcal{CFP} ; here, μ and σ denote, respectively, the mean and standard deviation.

We conclude from Figs. 5 and 6 that fibrotic patterns with small values of b and with large values of β_0 are most arrhythmogenic. We show this explicitly for model-(B) realizations of \mathcal{DFI} in Fig. 7: In Fig. 7(a), we plot versus p_f the Betti numbers β_0 (blue) and β_1 (maroon), and the lacunarity parameter b (green); the light-green rectangle indicates the region in which there is significant re-entry with a significant value of $\langle N_r \rangle$. In Fig. 7(b) we plot, versus p_f , $N_r/\langle N_r \rangle$ (blue curve) and $n_r/\langle n_r \rangle$ (pink curve), where $n_r \equiv \beta_0/b$; these curves (blue and pink) are correlated to the extent that they are large in the same range of values of p_f .

Earlier computational studies of cardiac-tissue fibrosis include Refs. [13, 22, 23, 31–35]; these are, roughly speaking, of two different types: (A) those that model the myocyte-fibroblast coupling [22, 23, 31–33]; and (b) those

that use geometrical modeling for \mathcal{DF} tissue [13, 34, 35]. There have been no studies, heretofore, which have investigated arrhythmogenesis, systematically and simultaneously, in all four types of fibrotic tissue. Our study leads to a natural way of quantifying the arrhythmogenicity of diffuse fibrosis (\mathcal{DF}), interstitial fibrosis (\mathcal{IF}), patchy fibrosis (\mathcal{PF}), and compact fibrosis (\mathcal{CF}) in cardiac tissue. We have shown that the statistical properties of these fibrotic-tissue patterns, such as their fractal dimension \mathbb{D} , lacunarity parameter b , and Betti numbers β_0 and β_1 are important in determining the arrhythmogenicity of fibrotic tissue. Our work sets the stage for (a) to experimental investigations of arrhythmogenesis in \mathcal{DF} , \mathcal{IF} , \mathcal{PF} , and \mathcal{CF} and (b) *in silico* studies of such studies that go beyond our model by using anatomically realistic simulation domains, with muscle-fiber orientation, realistic myocyte-fibroblast couplings, and bidomain models.

ACKNOWLEDGMENTS

MKM and RP thank Jaya Kumar Alageshan for discussions, the Department of Science and Technology (DST), India, and the Council for Scientific and Industrial Research (CSIR), India, for financial support, and the Supercomputer Education and Research Centre (SERC, IISc) for computational resources. BAJL thank the Australian Research Council for financial support (Grant no:CE140100049).

-
- [1] T. Kawara, R. Derksen, J. R. de Groot, R. Coronel, S. Tasseron, A. C. Linnenbank, R. N. Hauer, H. Kirkels, M. J. Janse, and J. M. de Bakker, *Circulation* **104**, 3069 (2001).
- [2] A. Biernacka and N. G. Frangogiannis, *Aging and disease* **2**, 158 (2011).
- [3] T. P. Nguyen, Z. Qu, and J. N. Weiss, *Journal of molecular and cellular cardiology* **70**, 83 (2014).
- [4] S. Hinderer and K. Schenke-Layland, *Advanced drug delivery reviews* **146**, 77 (2019).
- [5] SCA Foundation, “SCD statistics,” <https://www.sca-aware.org/sca-news/aha-releases-latest-statistics-on-sudden-cardiac-arrest>
- [6] E. R. Stormholt, J. Svane, T. H. Lyng, and J. Tfelt-Hansen, *Current Cardiology Reports* **23**, 1 (2021).
- [7] E. Baldi, G. M. Sechi, C. Mare, F. Canevari, A. Brancaglione, R. Primi, C. Klersy, A. Palo, E. Contri, V. Ronchi, *et al.*, *New England Journal of Medicine* **383**, 496 (2020).
- [8] K.-H. Kuck, *Herz* **45**, 325 (2020).
- [9] R. Mehra, *Journal of electrocardiology* **40**, S118 (2007).
- [10] M. Rubart, D. P. Zipes, *et al.*, *The Journal of clinical investigation* **115**, 2305 (2005).
- [11] M. Hocini, S. Y. Ho, T. Kawara, A. C. Linnenbank, M. Potse, D. Shah, P. Jaïs, M. J. Janse, M. Haïssaguerre, and J. M. De Bakker, *Circulation* **105**, 2442 (2002).
- [12] G. Balaban, B. P. Halliday, C. Mendonca Costa, W. Bai, B. Porter, C. A. Rinaldi, G. Plank, D. Rueckert, S. K. Prasad, and M. J. Bishop, *Frontiers in physiology* **9**, 1832 (2018).
- [13] R. Majumder, A. R. Nayak, R. Pandit, *et al.*, *PLOS ONE* **7**, 1 (2012).
- [14] R. Morgan, M. A. Colman, H. Chubb, G. Seemann, and O. V. Aslanidi, *Frontiers in physiology* **7**, 474 (2016).
- [15] F. Jousset, A. Maguy, S. Rohr, and J. P. Kucera, *Frontiers in physiology* **7**, 496 (2016).
- [16] R. H. Clayton, *Frontiers in physiology* **9**, 1052 (2018).
- [17] B. J. Hansen, J. Zhao, and V. V. Fedorov, *JACC: Clinical Electrophysiology* **3**, 531 (2017).
- [18] D. Jakes, K. Burrage, C. C. Drovandi, P. Burrage, A. Bueno-Orovio, R. W. dos Santos, B. Rodriguez, and B. A. Lawson, *BioRxiv*, 668848 (2019).
- [19] E. de la Calleja and R. Zenit, “Fractal dimension and topological invariants as methods to quantify complexity in Yayoi Kusama’s paintings,” (2020), arXiv:2012.06108 [nlin.PS].
- [20] D. J. Gould, T. J. Vadakkan, R. A. Poché, and M. E. Dickinson, *Microcirculation* **18**, 136 (2011).
- [21] K. H. Ten Tusscher and A. V. Panfilov, *American Journal of Physiology-Heart and Circulatory Physiology* **291**, H1088 (2006).
- [22] S. Zlochiver, V. Munoz, K. L. Vikstrom, S. M. Taffet, O. Berenfeld, and J. Jalife, *Biophysical journal* **95**, 4469 (2008).

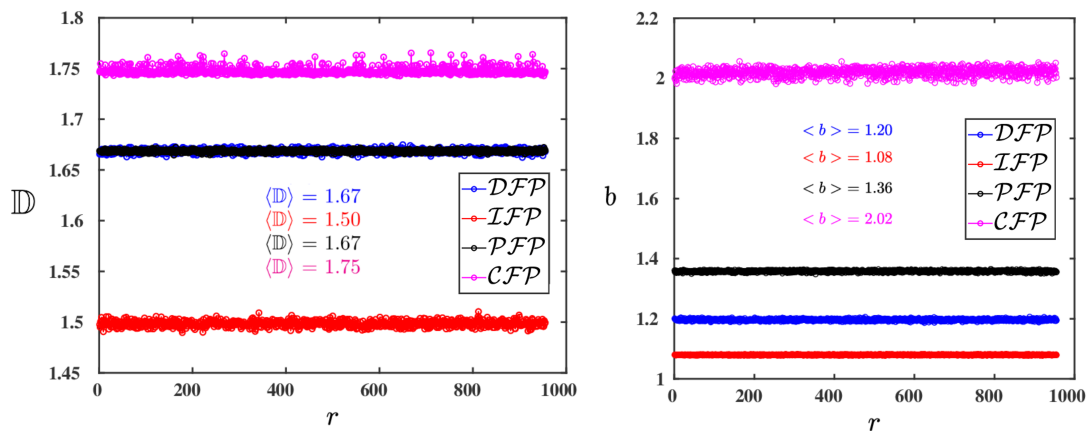


FIG. 5. (Color online) Plots versus the realisation number $r = 1, 2, \dots, 955$, for the Perlin-noise model (A), of the fractal dimension \mathbb{D} (left panel) and the lacunarity parameter b (right panel) in Eq. 4 fibrotic regions of types DFP (blue), IFP (red), PFP (black), and CFP (pink); we use angular brackets for mean values.

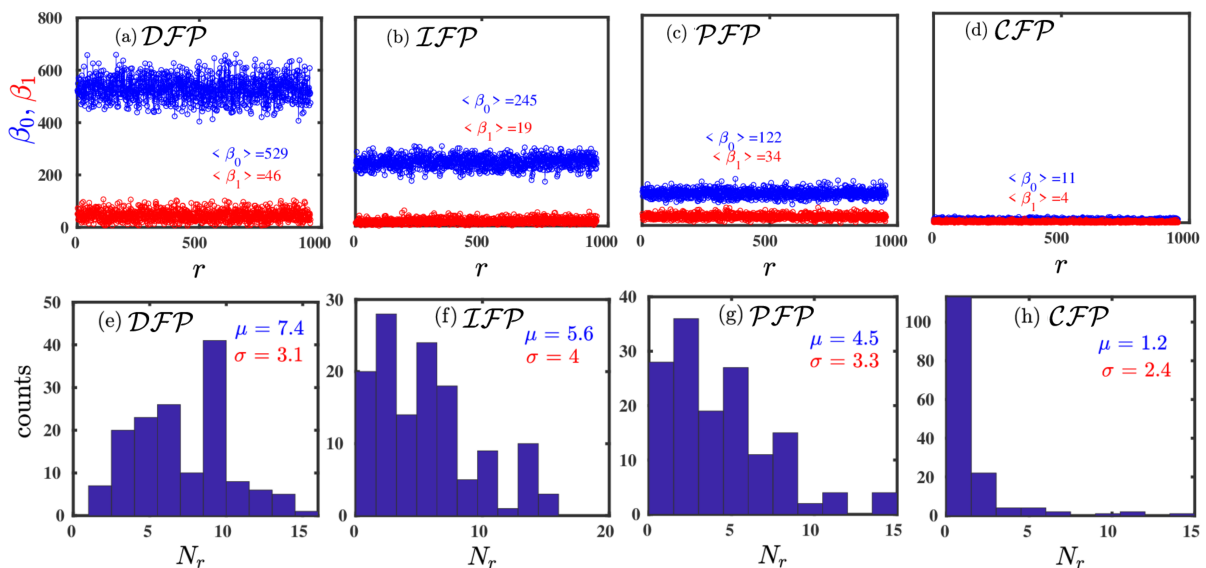


FIG. 6. (Color online) Plots versus the realisation number $r = 1, 2, \dots, 955$, for the Perlin-noise model (A), of the Betti numbers β_0 (blue) and β_1 (red) for (a) DFP , (b) IFP , (c) PFP , and (d) CFP ; we use angular brackets for mean values. Histograms of N_r , for 150 model-(B) realizations of fibrotic regions, for (e) DFP , (f) IFP , (g) PFP , and (h) CFP ; μ and σ are, respectively, the mean and standard deviation.

- [23] K. S. McDowell, H. J. Arevalo, M. M. Maleckar, and N. A. Trayanova, *Biophysical Journal* **101**, 1307 (2011).
 [24] Supplemental Material.
 [25] Pinta, “Pinta: Painting Made Simple,” <https://www.pinta-project.com/>.
 [26] R. Majumder, R. Pandit, and A. V. Panfilov, *American Journal of Physiology-Heart and Circulatory Physiology* **307**, H1024 (2014).
 [27] S. Zimik and R. Pandit, *Scientific reports* **7**, 1 (2017).
 [28] C. R. Tolle, T. R. McJunkin, and D. J. Gorsich, *Physica D: Nonlinear Phenomena* **237**, 306 (2008).
 [29] A. L. Karperien and H. F. Jelinek, *Frontiers in bioengineering and biotechnology* **3**, 51 (2015).
 [30] CHomP, “Computational Homology Software,” http://chomp.rutgers.edu/Projects/Computational_Homology/OriginalCHomP/software/.
 [31] Y. Xie, A. Garfinkel, P. Camelliti, P. Kohl, J. N. Weiss, and Z. Qu, *Heart Rhythm* **6**, 1641 (2009).
 [32] A. R. Nayak, T. Shajahan, A. Panfilov, and R. Pandit, *PloS one* **8**, e72950 (2013).
 [33] A. R. Nayak and R. Pandit, *Physical Review E* **92**, 032720 (2015).
 [34] K. H. Ten Tusscher and A. V. Panfilov, *Europace* **9**, vi38 (2007).
 [35] S. Alonso, R. W. dos Santos, and M. Bär, *PloS one* **11**, e0166972 (2016).

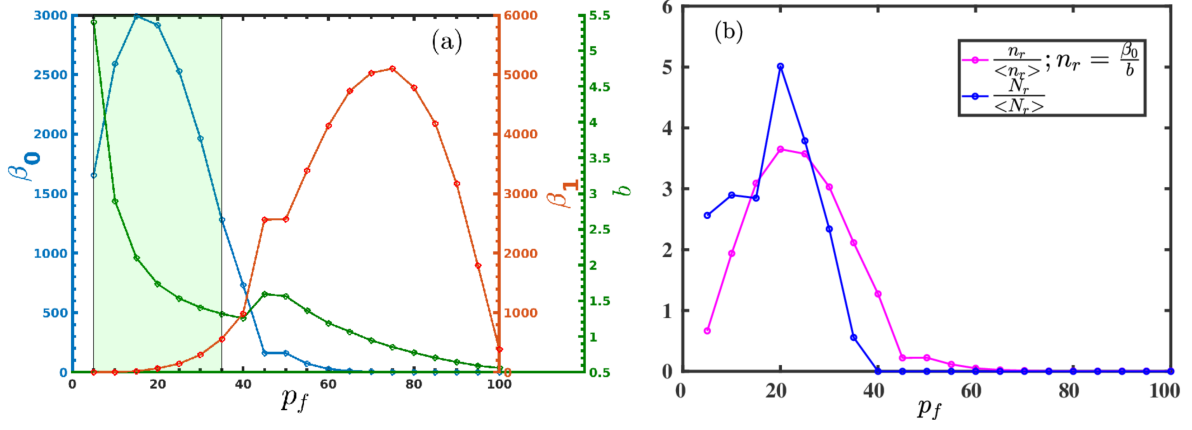


FIG. 7. (Color online) Plots versus p_f : (a) the Betti numbers β_0 (blue) and β_1 (maroon) and the lacunarity parameter b (green); the light-green rectangle indicates the region in which $\langle N_r \rangle$ is significant; (b) $N_r / \langle N_r \rangle$ (blue curve) and $n_r / \langle n_r \rangle$ (pink curve).

Supplementary Material: Arrhythmogenicity of cardiac fibrosis: fractal measures and Betti numbers

Mahesh Kumar Mulimani,^{1,*} Brodie A. J. Lawson,^{2,3,†} and Rahul Pandit^{1,‡}

¹Centre for Condensed Matter Theory, Department of Physics,
Indian Institute of Science, Bangalore 560012, India.

²Centre for Data Science, Queensland University of Technology, Brisbane, Australia.

³ARC Centre of Excellence for Mathematical and Statistical Frontiers,
Queensland University of Technology, Brisbane, Australia.

PACS numbers: 87.19.Xx, 87.15.Aa

We give below the following supplementary information, which is mentioned in the main paper:

1. We can characterize 2D fibrotic textures by their Betti numbers [1] β_0 and β_1 , which measure, respectively, the number of connected components and the number of holes that are completely enclosed by occupied pixels (see Fig. S1). To obtain β_0 and β_1 , we convert the fibrotic-tissue data sets into the bit-map (bmp) image format; and then we use the computational-homology-project software [2] to get β_0 and β_1 for the particular fibrotic image.
2. In Fig. S2 we present histograms of the Betti numbers β_0 and β_1 , in fibrotic tissue with diffuse fibrosis (DFP), interstitial fibrosis (IFP), patchy fibrosis (PFP), and compact fibrosis (CFP); we use the Perlin-noise [3] model (A) [see the main paper] and 955 different realizations for each type of region, namely, DF , IF , PF , and CF .
3. In Fig. S3 we present the following scatter plots, in fibrotic tissue with diffuse fibrosis (DFP), interstitial fibrosis (IFP), patchy fibrosis (PFP), and compact fibrosis (CFP); we use the Perlin-noise [3] model (A) [see the main paper] and 955 different realizations for each type of region, namely, DFP , IFP , PFP , and CFP : (a) the lacunarity parameter b and the Betti numbers β_0 , and β_1 ; (b) β_0 and β_1 ; and (c) b and β_1 .
4. In Figs. S4 (a)-(c) we present three representative images of diffuse fibrosis (DFP); we use the Perlin-noise [3] model (A) [see the main paper]. In Fig. S4 (d) we plot, for each one of the images, the lacunarity $\mathcal{L}(\epsilon)$ versus the box length ϵ [see Eq. (3) in the main paper], and, by using Eq. (4) in the main paper, we obtain the lacunarity parameter b .
5. In Fig. S5 we assess the quality of the fit, given Eq.(4) in the main paper, by plotting the lacunarity $\mathcal{L}(\epsilon)$ versus the box length ϵ [see Eq. (3) in the main paper]. First row: for the Perlin-noise [3] model (A) [see the main paper] for (a) DFP , (b) IFP , (c) PFP , and (d) CFP ; second row: for the idealised model (B) [see the main paper] for (e) DFI , (f) IFI , (g) PFI , and (h) CFI . From such plots we obtain the lacunarity parameter b ; clearly, this fit is not very good in some cases, especially for CFI , CFP (but, even for this case, the mean value of R^2 , the goodness of fit, is 81.4%).
6. In Fig. S6 we present representative pseudocolor plots of the transmembrane potential V_m which show that there is no arrhythmogenesis if we use only (i) fibrotic tissue with no remodelling of myocytes or (ii) a remodelled region with no fibrotic tissue.

-
- [1] E. de la Calleja and R. Zenit, *Fractal dimension and topological invariants as methods to quantify complexity in yayoi kusama's paintings* (2020), 2012.06108.
 - [2] CHomP, *Computational Homology Software*, http://chomp.rutgers.edu/Projects/Computational_Homology/OriginalCHomP/software/.
 - [3] D. Jakes, K. Burrage, C. C. Drovandi, P. Burrage, A. Bueno-Orovio, R. W. dos Santos, B. Rodriguez, and B. A. Lawson, *BioRxiv* p. 668848 (2019).

*Electronic address: maheshk@iisc.ac.in ;

†Electronic address: brodie.lawson86@gmail.com ;

‡Electronic address: rahul@iisc.ac.in;

also at Jawaharlal Nehru Centre For Advanced Scientific Research, Jakkur, Bangalore, India

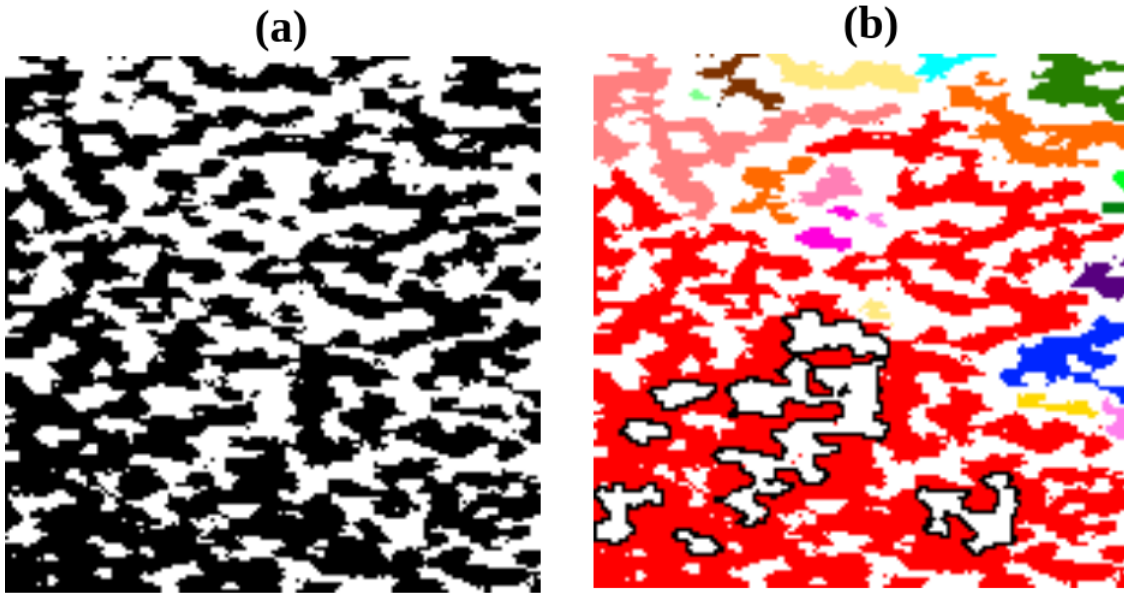


FIG. S1: (Color online) The computation of β_0 and β_1 , which measure, respectively, the number of connected components and the number of holes that are completely enclosed by occupied pixels. To obtain β_0 and β_1 , we convert the fibrotic-tissue data sets into the bit-map (bmp) image format; and then we use the computational-homology-project software [2] to get β_0 and β_1 for the particular fibrotic image. (a) A representative image for a region with diffuse fibrosis \mathcal{DFP} in the Perlin-noise model (A) [see the main paper]. (b) A colored version of the image in (a), with different colors for the major, distinct, connected components; we have drawn black boundaries for a few, representative, holes, which are completely enclosed by occupied pixels; by identifying such connected components and fully enclosed holes, we obtain the Betti numbers; a careful computation for this image yields $\beta_0 = 35$ and $\beta_1 = 72$.

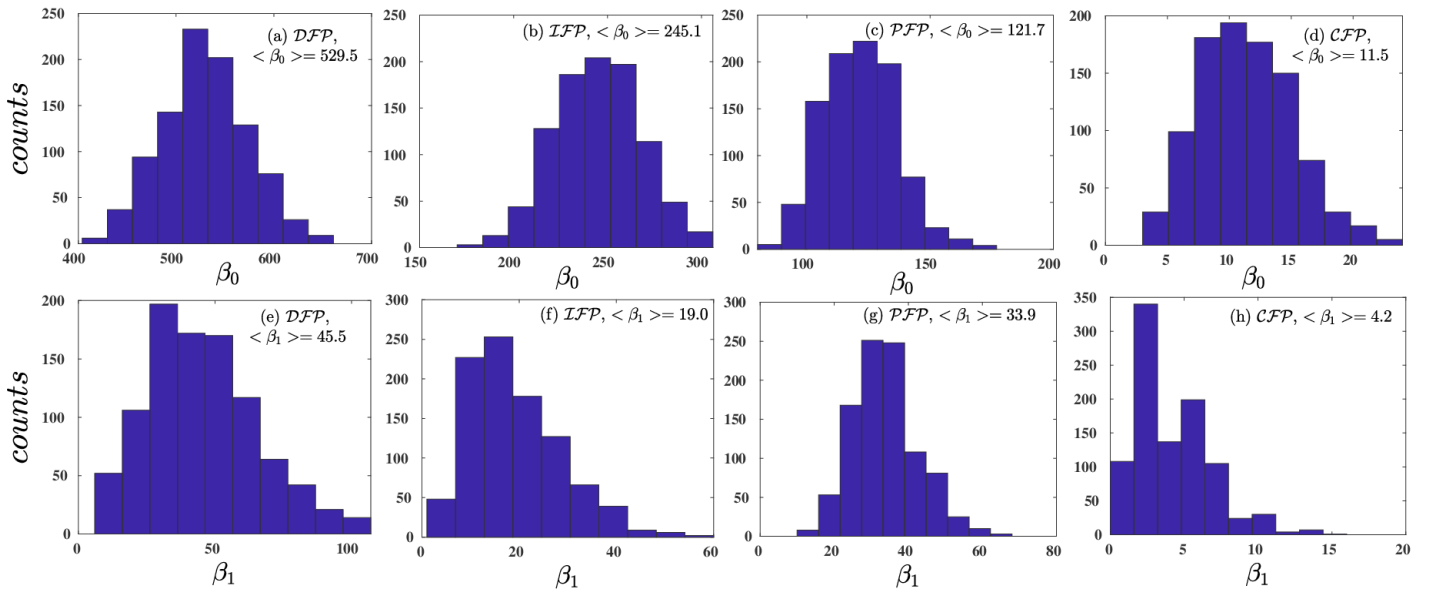


FIG. S2: (Color online) Histograms of Betti numbers, from 955 different fibrotic-tissue realizations for every fibrotic type.

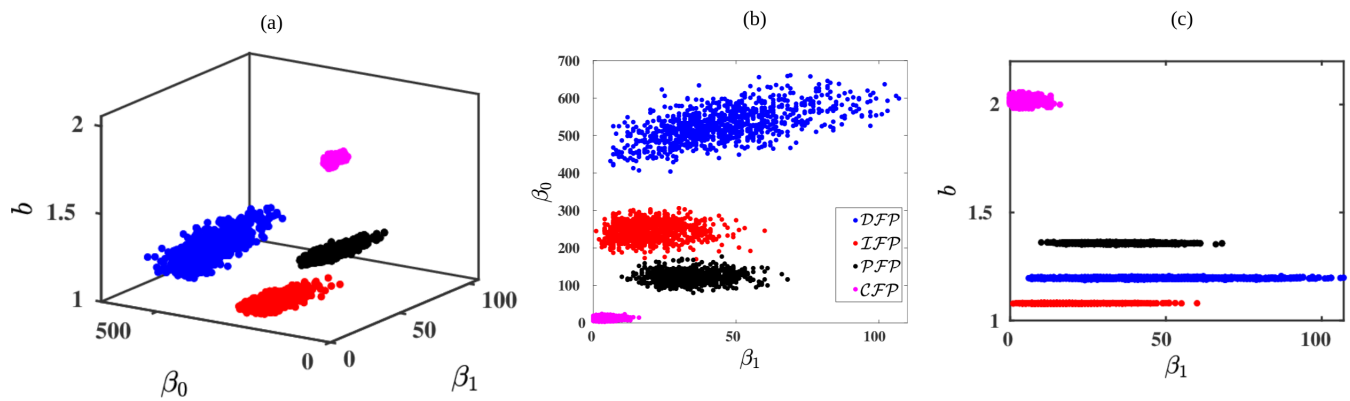


FIG. S3: (Color online) Scatter plots, in fibrotic tissue with diffuse fibrosis (DFP), interstitial fibrosis (IFP), patchy fibrosis (PFP), and compact fibrosis (CFP); we use the Perlin-noise [3] model (A) (see the main paper) and 955 different realizations for each type of region, namely, DFP , IFP , PFP , and CFP : (a) the lacunarity parameter b and the Betti numbers β_0 , and β_1 ; (b) β_0 and β_1 ; and (c) b and β_1 .

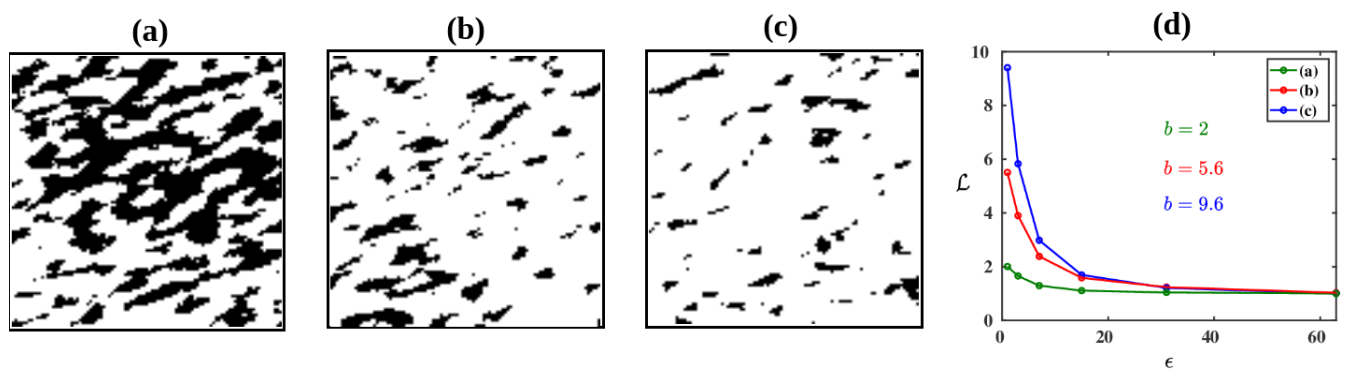


FIG. S4: (Color online) Three representative images (a)-(c) of diffuse fibrosis (DFP); we use the Perlin-noise [3] model (A) [see the main paper]. (d) Plots, for each one of the images (a)-(c), of the lacunarity $\mathcal{L}(\epsilon)$ versus the box length ϵ [see Eq. (3) in the main paper]; by using Eq. (4) in the main paper, we obtain the lacunarity parameter b .

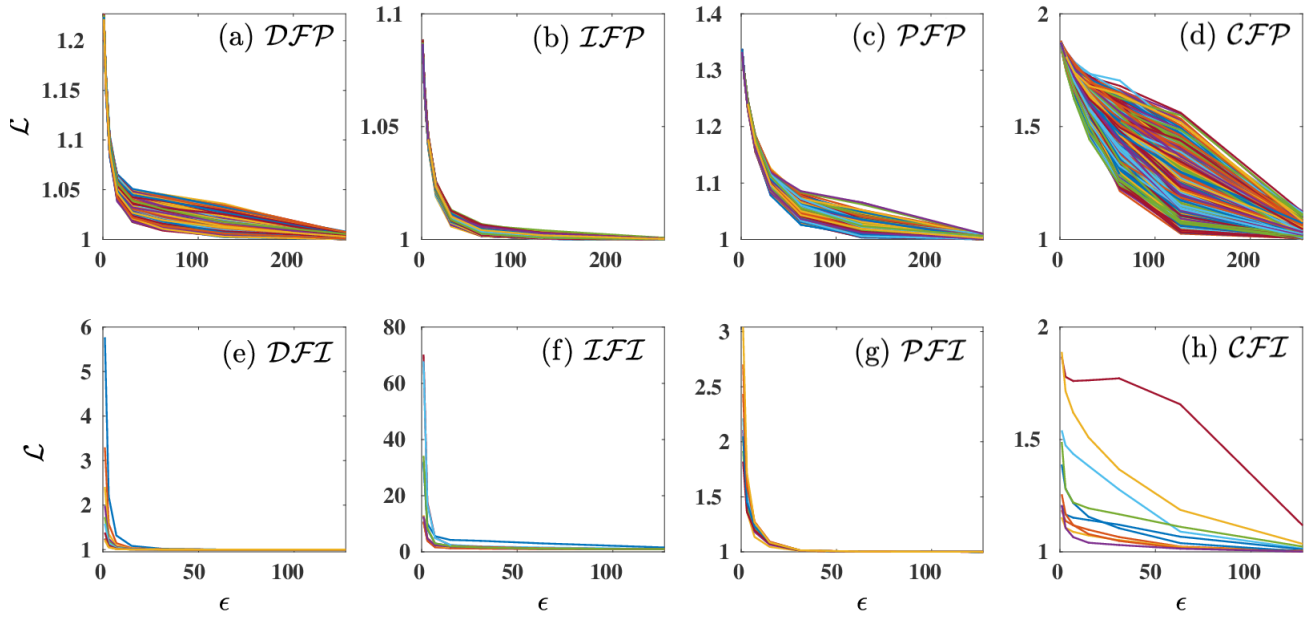


FIG. S5: (Color online) We assess the quality of the fit, given Eq.(4) in the main paper, by plotting the lacunarity $\mathcal{L}(\epsilon)$ versus the box length ϵ [see Eq. (3) in the main paper]. First row: for the Perlin-noise [3] model (A) [see the main paper] for (a) \mathcal{DFP} , (b) \mathcal{IFP} , (c) \mathcal{PFP} , and (d) \mathcal{CFP} ; second row: for the idealised model (B) [see the main paper] for (e) \mathcal{DFI} , (f) \mathcal{IFI} , (g) \mathcal{PFI} , and (h) \mathcal{CFI} . From such plots we obtain the lacunarity parameter b ; clearly, this fit is not a good one in some cases, especially for \mathcal{CFP} , \mathcal{CFI} (but, even for this case, the mean value of R^2 , the goodness of fit, is 81.4%).

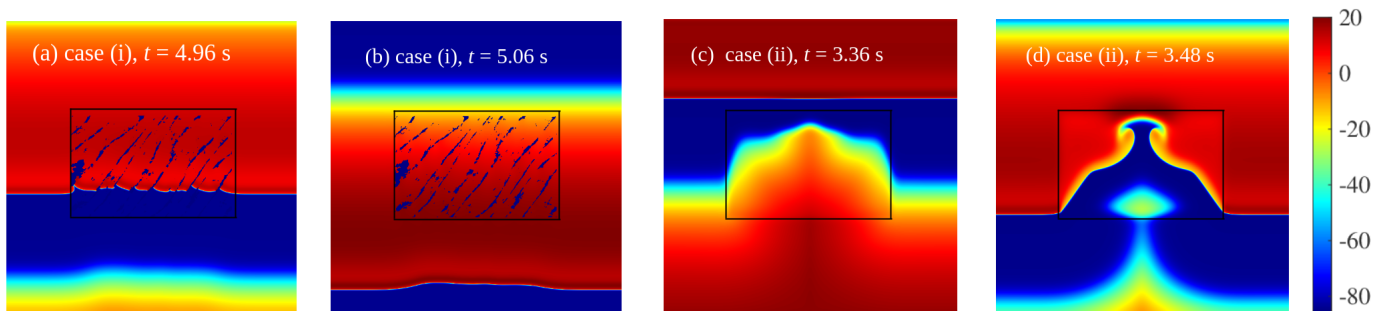


FIG. S6: (Color online) Representative pseudocolor plots of the transmembrane potential V_m which show that there is no arrhythmogenesis if we use only (i) fibrotic tissue with no remodelling of myocytes or (ii) a remodelled region with no fibrotic tissue.